

# Simultaneously enhancing brightness and purity of WSe<sub>2</sub> single photon emitter using high-aspect-ratio nanopillar array on metal

Mayank Chhaperwal<sup>1</sup>, Himanshu Madhukar Tongale<sup>1</sup>, Patrick Hays<sup>2</sup>, Kenji Watanabe<sup>3</sup>,  
Takashi Taniguchi<sup>4</sup>, Seth Ariel Tongay<sup>2</sup> and Kausik Majumdar<sup>1\*</sup>

<sup>1</sup>Department of Electrical Communication Engineering,  
Indian Institute of Science, Bangalore 560012, India

<sup>2</sup>Materials Science and Engineering, School for Engineering of Matter, Transport and Energy,  
Arizona State University, Tempe, Arizona 85287, USA

<sup>3</sup>Research Center for Electronic and Optical Materials,  
National Institute for Materials Science, 1-1 Namiki, Tsukuba 305-044, Japan

<sup>4</sup>Research Center for Materials Nanoarchitectonics,  
National Institute for Materials Science, 1-1 Namiki, Tsukuba 305-044, Japan

\*Corresponding author, email: kausikm@iisc.ac.in

## Abstract

Monolayer semiconductor transferred on nanopillar arrays provides site-controlled, on-chip single photon emission, which is a scalable light source platform for quantum technologies. However, the brightness of these emitters reported to date often falls short of the perceived requirement for such applications. Also, the single photon purity usually degrades as the brightness increases. Hence, there is a need for a design methodology to achieve enhanced emission rate while maintaining high single photon purity. Using WSe<sub>2</sub> on high-aspect-ratio ( $\sim 3$  - at least two-fold higher than previous reports) nanopillar arrays, here we demonstrate  $> 10$  MHz single photon emission rate in the 770-800 nm band that is compatible with quantum memory and repeater networks (Rb-87-D1/D2 lines), and satellite quantum communication. The emitters exhibit excellent purity (even at high emission rates) and improved out-coupling due to the use of a gold back reflector that quenches the emission away from the nanopillar.

**keywords:** Single photon source, quantum emitter, WSe<sub>2</sub>, 2D materials, brightness, second order correlation.

On-chip single photon emitters (SPEs) provide a scalable approach towards photonics-based quantum technologies such as quantum computing, quantum communication, and quantum metrology [1,2]. SPEs based on transition metal dichalcogenides (TMDCs) are highly attractive as the two-dimensional nature of the host provides several possible advantages, such as, ease of integration with photonic/plasmonic cavities and waveguides [3–8], low outcoupling loss [3,5–7], gate induced spectral tunability [9–12], and the possibility of integration with electrical excitation scheme [11,13,14]. In nanopillar-based SPE implementations, the strain introduced on the monolayer through a nanopillar helps funnel excitons [15–19] toward the defect located at the pillar site, improving the net quantum efficiency of single photon emission [20,21]. While such sources are highly promising due to the spatially deterministic nature of the array of quantum emitters at the lithographically defined positions [4, 8, 9, 20–23], there are two key challenges that must be addressed for practical quantum applications.

These two challenges are illustrated in Figure 1, where we plot the measured brightness (in counts per second) as a function of single photon purity [in terms of  $g^{(2)}(0)$ ] for reported TMDC-based SPEs [3–5,8,24–26]. The first observation is that the overall brightness is, in general, low, both with respect to other competing technologies (for example, quantum dots exhibiting several tens of MHz [27–29]) as well as the perceived requirement for several quantum technologies (in GHz, see [29,30]). The emission intensity from TMDC-based SPEs usually saturates much earlier than the rate suggested by their lifetime. Auger annihilation has been suggested as the limiting factor for such early saturation [8]. While methods, such as photonic/plasmonic cavities [3,8], have improved the brightness of the SPEs, there is still a pressing need for further improvement.

While good single photon purity has been demonstrated in the past [20–22], the second observation from Figure 1 is the lack of reports with simultaneous observation of low  $g^{(2)}(0)$  and high emission rate. The diffraction-limited laser spot is much larger than the nanopillar diameter for optical excitation. This causes considerable contribution from the surrounding regions to the collected photon count. Unlike the SPE, the background emission is not bottlenecked by

a single level and, hence, does not have a strong saturating behavior with increasing power. Accordingly, it often starts to dominate the SPE emission at higher excitation power, degrading the single photon purity.

The aim of this work is to bridge the above-mentioned gaps by introducing high-aspect-ratio nanopillars on metal film to significantly improve the brightness of the TMDC-based SPEs while maintaining an excellent single photon purity at high emission rates - a step towards practical SPE solution for various quantum technologies.

Transferring a monolayer on a nanopillar introduces a non-uniform strain in the flake, with maximum strain at the pillar site. The band gap of the monolayer reduces with such local strain [15–17], causing excitons to funnel toward the pillar site. A point defect on the pillar captures these available excitons and emits subsequently, giving rise to single photon emission.

The overall design of our SPE array employing monolayer WSe<sub>2</sub> on nanopillars has three important features, as illustrated schematically in Figure 2a. The design is inspired by our model (discussed later) predicted brightness of the SPE as a function of Auger strength and pillar aspect ratio (height:diameter, denoted as  $\alpha$ ), shown in Figure 2b. The results suggest that Auger-induced exciton annihilation in the strain-induced potential well on the nanopillar prevents the SPE from achieving its lifetime-limited emission rate. However, a higher  $\alpha$  helps to overcome this limitation through stronger exciton funneling toward the pillar site (see inset of Figure 2a). One drawback of high-aspect-ratio nanopillars made of hard material, such as SiO<sub>2</sub>, having a rough top surface, is the possibility of piercing through the flake during the transfer process [21, 31]. To mitigate this, we fabricate the nanopillars using a negative photoresist followed by baking (see **Methods** in Supporting Information 1). The polymer-based negative resist provides a comparatively softer structure and a smoother top surface. We fabricate an array of such nanopillars, keeping a pillar-to-pillar spacing (5  $\mu\text{m}$ ) well beyond the excitation laser spot size ( $\sim 1.5 \mu\text{m}$ ) so that only one pillar is excited at a time (top panel of Figure 2c for a schematic view and the bottom panel for an optical image). Figure 2d shows an SEM image of a single nanopillar with WSe<sub>2</sub> monolayer on top. The inset is an SEM image of a bare nanopillar with a diameter of about 110 nm. AFM measurement indicates a height of about 330 nm (Figure 2e). This gives us  $\alpha \sim 3$ , significantly higher than previous reports [20–22].

Secondly, encapsulating TMDCs with hBN smoothens the inhomogeneous potential fluctuation and screens the inter-exciton interaction. This reduces the Auger coefficient significantly through suppressed interaction among locally trapped excitons [32–34]. Accordingly, we transfer a few-layer hBN flake on top of the monolayer/nanopillar stack. However, no hBN layer is introduced between the monolayer and the nanopillar to avoid a possible reduction in the strain.

Finally, in order to improve single photon purity, we mitigate the issue of the laser excitation spot being much larger than the nanopillar area by fabricating the nanopillars on gold-coated substrate. The part of the monolayer away from the nanopillar touches the gold film (Figure 2a), and the emission from those regions is almost completely quenched due to non-radiative charge transfer to gold [35]. This allows us to collect the emission only from the nanopillar region selectively. To support this claim, we perform a photoluminescence (PL) scan on the sample at 295 K around the free exciton emission energy (excited using 532 nm laser), and the integrated emission intensity is overlaid on the optical image (bottom panel of Figure 2c). The bright emission spots coincide with the location of the nanopillars in the optical image. A line cut from the PL map is presented in Supporting Information 2. The emission from the flake away from the nanopillar is almost completely quenched. On the other hand, excitons funnel to the nanopillar locations from the suspended regions, providing high brightness at the pillar site (schematic in Figure 2a). Most of the pillars covered by the monolayer show bright emission, suggesting high yield and minimal damage to the flake during the transfer process. Finally, the gold-coating acts as a back-reflector, improving the out-coupling of the emitted photons as depicted from the simulated emission pattern (Figure 2f) using 2D finite-difference time-domain (FDTD) method.

We refer to this SPE stack (with  $\alpha = 3$ ) as structure S1 and prepare three different samples (S1-A, S1-B, and S1-C) containing arrays of nanopillars.

Figure 3a (left panel) shows representative PL emission spectra from four different nanopillars. The vertical dashed lines indicate the spectral position of the defect emission functioning as an SPE around 1.55 - 1.61 eV. The corresponding emission wavelength is in the 770-800 nm band and is thus suitable for quantum memory and repeater networks (being close to the

Rb-87-D1/D2 line) [36] and satellite communication applications [37]. Note that the SPE peak is red-shifted compared to the broad defect and multi-particle emission of WSe<sub>2</sub> and, thus, is relatively free from background emission. Figure 3a (right panel) shows a high ( $\sim 92\%$ ) degree of linear polarization (DOLP) of these peaks. The DOLP value remains independent of the direction of the polarization of the excitation, suggesting the intrinsic linearly polarized nature of the SPE.

The SPE peak intensity strongly depends on the excitation wavelength. As an example, we choose an emitter around 1.59 eV and find that the peak intensity is highest when the excitation is resonant to the WSe<sub>2</sub> free exciton (Figure 3b).

The sharpest peak we measured has a full-width-at-half-maximum (FWHM) of 520  $\mu\text{eV}$  and is shown in Figure 3c. We perform incident power ( $P$ ) dependent PL measurement to characterize the brightness of the SPE. Figure 3c shows the method used to calculate the emission rate of the SPE. The peaks are fitted using a Voigt function, and the contributions from the side peaks and the background are removed. The SPE peak is then integrated within its FWHM (marked by the shaded portion) and then adjusted for our system efficiency of 5.1%. This integrated emission intensity ( $I$ ) of the SPE peak is plotted against  $P$  in Figure 3d, and the data is fitted with  $I = I_{sat} \cdot \{P/(P + P_{sat})\}$ . This gives us a maximum emission rate of  $10.53 \pm 0.22$  MHz, which is free from other spurious contributions. Note that we deliberately do not report the collected SPAD count rate. This is because even after spectral filtering, the photons collected by the SPAD have a component arising from the background and side peaks. This component increases rapidly with the incident power and thus results in erroneous inflation of the measured emission rate of the device (Supporting Information 3). Power dependent emission rate from three other fabrication runs is shown in Supporting Information 4, suggesting a repeatable high emission rate from our samples.

Note that this is the emission rate collected by the objective [numerical aperture (NA) of 0.5] and is not corrected for the collection angle limited by its NA. Our FDTD simulation (Figure 2f) predicts that 33.93% of the total photons emitted by the dipole above the substrate surface are collected by our objective. This gives an emission rate of  $\sim 31$  MHz above the surface of the substrate. Collection efficiency with respect to the total emission is 28.36%, giving a total emission rate of  $\sim 37$  MHz. The FDTD simulation also rules out the existence of

Purcell enhancement in the structure.

We perform time-resolved photoluminescence (TRPL) measurement to characterize the lifetime [5, 6, 14, 20, 21, 25, 38–42] of the trapped exciton in the quantum emitter (Figure 3e). After fitting with a decaying exponential convoluted with a Gaussian rise function (see **Methods** in Supporting Information 1), we extract a lifetime ( $\tau_d$ ) of  $487.15 \pm 0.84$  ps and a formation time ( $\tau_f$ ) of  $541 \pm 0.95$  ps.

To characterize the single photon nature of the emission, we perform second-order correlation measurement in a Hanbury Brown and Twiss (HBT) setup. After deconvolution from the Gaussian instrument response function (IRF) (see **Methods** in Supporting Information 1), we extract a  $g^{(2)}(0)$  value of  $0.113 \pm 0.015$  at a high collected count rate of 1 MHz. Note that the fit does not involve any background correction. The maintained single photon purity at this high emission rate confirms the functioning of the gold-coated substrate as an excellent background suppressor. Spectral separation of the SPE from typical broad defect emission of WSe<sub>2</sub> also helps because the tail of such broad emission does not intrude into the spectral region of the SPE. The corresponding  $g^{(2)}(\tau)$  plot for the sample exhibiting the narrowest SPE peak (spectrum in Figure 3c) is shown in Supporting Information 5. Also, in Supporting Information 6, we show  $g^{(2)}(\tau)$  from a lower-aspect-ratio pillar (sample S2) with a  $g^{(2)}(0)$  of  $0.024 \pm 0.017$ .

In Figure 1, we compare our results with reported data [3–5, 8, 24–26] in the space of maximum emission rate versus  $g^{(2)}(0)$ , suggesting a superior emission rate while maintaining improved single photon purity. The emission rate from our high aspect-ratio pillars is 7-fold higher than the previous highest reported rate from pillars without cavities and is on par with works using photonic/plasmonic cavities.

We model the SPE as two interconnected subsystems (see Figure 4a): (a) exciton funneling in the strain-induced potential well, and (b) these funneled excitons acting as a reservoir for exciting the defect-based atom-like two-level system, which then relaxes to the ground state, emitting single photons. We discuss these two parts of the model below.

The rate equation for the exciton density  $n(r, t)$  at a radial distance  $r$  from the center of

the strain well is given by (see Supporting Information 7 for derivation):

$$\frac{\partial n(r, t)}{\partial t} = -\frac{\partial F(r)}{\partial r} + g(r) - \frac{n(r)}{\tau_e} - \gamma n^2(r) \quad (1)$$

Here the first term on the right-hand side captures both the out-diffusion of excitons due to concentration gradient and the drift of excitons towards the pillar center due to strain gradient,  $F$  being the total outward flux of the excitons.  $g(r)$  is the generation rate with a spatial Gaussian profile,  $\tau_e$  is the effective lifetime of the exciton (combining both radiative and non-radiative pathways, other than Auger process) and  $\gamma$  is the Auger coefficient.

The calculated steady-state ( $\frac{\partial n(r, t)}{\partial t} = 0$ ) exciton density profile [ $n(r)$ ] is plotted in Figure 4b, suggesting stronger exciton funneling as  $\alpha$  increases. In Figure 4c, we plot the total exciton population [ $N_x = \int_0^{r_0} 2\pi r n(r) dr$ ] near the center of the nanopillar as a function of  $P$  for different  $\gamma$  ( $r_0$  is taken as 1 nm in the plots). The results indicate a saturation in  $N_x$  with  $P$ , and  $N_x$  saturates at a lower value for higher  $\gamma$ . This suggests that Auger annihilation, being a quadratic function, is the primary bottleneck to increase  $N_x$ . A higher  $\alpha$  that induces stronger exciton funneling could be a way to mitigate such Auger-mediated saturation, as illustrated in Figure 4d.

An exciton from the reservoir that is in the vicinity is captured by a point defect, populating an atom-like two-level system consisting of the defect state and the ground state (Figure 4a). The SPE emission energy is  $\sim 200$  meV lower than the free exciton (Figure 3a). The hybridization of this defect state with the dark exciton band [43–47] is thus unlikely in our samples because of the large energy separation between them.

The steady-state emission rate of the SPE is given by (see Supporting Information 9 for derivation):

$$I_{SPE} = \Gamma_{dr} \left( \frac{N_x \Gamma_{trap}}{N_x \Gamma_{trap} + \Gamma_d} \right) \quad (2)$$

Here  $\Gamma_{trap}$  quantifies the rate of capture of an individual exciton by the defect.  $\Gamma_d = \frac{1}{\tau_d} = \Gamma_{dr} + \Gamma_{dnr}$  is the effective rate of relaxation from the defect state, considering both radiative ( $\Gamma_{dr}$ ) and non-radiative ( $\Gamma_{dnr}$ ) pathways. In Figure 4e, the calculated  $I_{SPE}$  is plotted against incident power for varying  $\alpha$ , indicating an effective enhancement of the maximum emission rate with pillar aspect ratio. The variation of the calculated maximum emission rate is shown earlier (Figure 2b) in a colour plot as a function of the Auger coefficient and pillar aspect ratio.

To verify that such a high emission rate results from the increased strain due to the higher aspect ratio of our nanopillars, we prepare two other samples (S2 and S3) with a lower aspect ratio of  $\alpha = 0.27$  and  $\alpha = 0.88$  respectively. The maximum collected rate measured from these devices is plotted in Figure 4f. The model provides an excellent fit to the experimentally observed maximum emission rate as a function of  $\alpha$ , verifying the validity of the model.

Note that  $N_x\Gamma_{trap}$  provides a good estimate of the rate of formation of the defect-bound exciton (see Supporting Information 8-9), and hence  $N_x\Gamma_{trap} \approx \frac{1}{\tau_f}$ . With this approximation, Equation 2 reduces to the expected form:

$$I_{SPE} = \eta \times \frac{1}{\tau_f + \tau_d} \quad (3)$$

Here  $\eta = \frac{\Gamma_{dr}}{\Gamma_d}$  is the quantum efficiency of the defect emission.

Equations 2 and 3 provide key insights into the possible ways to enhance the SPE emission rate, and the results are shown in Figure 4g. For example, when  $N_x\Gamma_{trap} \ll \Gamma_d$ , that is, when the defect state is starved of exciton supply from the reservoir (lower half in Figure 4g, denoted as ‘*supply-limited*’),  $I_{SPE} \approx \eta N_x\Gamma_{trap} \approx \eta/\tau_f$  and hence  $I_{SPE}$  exactly follows  $N_x$ . Since  $N_x$  saturates at higher excitation power,  $I_{SPE}$  also saturates prematurely without reaching the true lifetime limited rate of  $\Gamma_{dr}$ . Such saturation behavior thus does not arise from the limit of a 2-level quantum system. We believe a majority of the reported TMDC-based SPEs to date fall under this regime. Mitigating the Auger-induced early saturation by increasing the nanopillar aspect ratio can improve the emission rate in this regime (see Figure 4e).

On the other hand, when  $N_x\Gamma_{trap} \gg \Gamma_d$ , that is, when the defect state is not starved by the supply of excitons (upper half in Figure 4g, denoted as ‘*lifetime-limited*’),  $I_{SPE} \approx \Gamma_{dr}$  indicating radiative lifetime-limited emission rate, and thus further increasing the supply through enhanced pillar aspect ratio or reducing Auger recombination is not effective anymore in this regime. This also means that with adequate supply,  $I_{SPE}$  can achieve  $\Gamma_{dr}$  irrespective of the value of  $\Gamma_{dnr}$ .

To verify the model, in Supporting Information 10, we compare the emission spectra of samples S1-A and S1-C. S1-C uses the same aspect ratio pillars ( $\alpha = 3$ ) as S1-A, however, a different batch of WSe<sub>2</sub> that exhibits relatively weak background emission. This suggests a smoother potential profile and, thus, likely suppressed Auger loss due to reduced exciton



localization [32–34]. The defect peak emission is slightly blue shifted to 1.6 eV in this sample. Interestingly, we achieve a similar maximum count rate of  $7.4 \pm 0.17$  MHz; however, the saturation excitation power ( $P_{sat}$ ) is  $\sim 35$ -fold lower compared with S1-A. By varying the Auger coefficient for S1-A and S1-C, our model provides an excellent fit (Figure 4h) with the experimentally obtained emission rate as a function of excitation power for both the samples.

The second factor on the right side in Equation 2, that is,  $\beta \equiv \frac{N_x \Gamma_{trap}}{N_x \Gamma_{trap} + \Gamma_d}$  provides a quantitative estimate of the degree of supply limitation, with  $\beta$  close to zero indicating strong supply limitation, and  $\beta$  close to unity indicating lifetime-limited regime. In our sample S1-A with a high pillar aspect ratio, the extracted values of  $\tau_f$  and  $\tau_d$  from TRPL suggest  $\beta \approx 0.47$ . This justifies the lack of a proportionate increment in the maximum emission rate in S1-C (with respect to S1-A) in spite of significant suppression of the Auger coefficient.

Finally, with the estimated total emission rate of  $\sim 37$  MHz and  $\beta \approx 0.47$ , Equation 2 suggests a radiative rate ( $\Gamma_{dr}$ ) of  $\sim 79$  MHz and hence a radiative lifetime of  $\sim 12.6$  ns. Thus, there is a scope for further optimization of the pillar aspect ratio to improve the maximum emission rate by nearly a factor of two. However, a significant enhancement in the emission rate beyond this would require improving  $\Gamma_{dr}$ , possibly through cavity and material design, which could lead to scalable and highly pure single photon emission with rates beyond 100 MHz. Further, in the current work, there is a lack of precise control on the SPE emission wavelength, which could be addressed in the future through an external electric field-induced Stark shift.

## Supporting Information

The Supporting Information is available free of charge at XXX on fabrication and characterization methods, line cut from PL mapping of emitters, SPAD count rate versus pure SPE count rate, emission rate data from additional samples, single photon purity data from additional samples, description of the model, a description of two-level emitter, SPE model details, comparison of devices with higher and lower Auger coefficients.

## Acknowledgements

K.M. acknowledges useful discussion with Naresh Babu Pendyala from ISRO. This work was supported in part by a Core Research Grant from the Science and Engineering Research Board (SERB) under Department of Science and Technology (DST), grants from Indian Space Research Organization (ISRO), a grant under SERB TETRA, a grant from I-HUB QTF, IISER Pune, and a seed funding under Quantum Research Park (QuRP) from Karnataka Innovation and Technology Society (KITS), K-Tech, Government of Karnataka. K.W. and T.T. acknowledge support from the JSPS KAKENHI (Grant Numbers 21H05233 and 23H02052) and World Premier International Research Center Initiative (WPI), MEXT, Japan. S. T. acknowledges direct support from DOE-SC0020653 (materials synthesis), NSF ECCS 2052527, DMR 2111812, and CMMI 2129412. The use of facilities within the Eyring Materials Center at Arizona State University is partly supported by NNCI-ECCS-1542160.

## Competing Interests

The authors declare no competing financial or non-financial interests.

## Data Availability

Data available on reasonable request from the corresponding author.

## References

- [1] Alejandro R.-P. Montblanch, Matteo Barbone, Igor Aharonovich, Mete Atatüre, and Andrea C. Ferrari. Layered materials as a platform for quantum technologies. *Nature Nanotechnology*, 18(6):555, June 2023.
- [2] Mikko Turunen, Mauro Brotons-Gisbert, Yunyun Dai, Yadong Wang, Eleanor Scerri, Cristian Bonato, Klaus D. Jöns, Zhipei Sun, and Brian D. Gerardot. Quantum photonics with layered 2D materials. *Nature Reviews Physics*, 4(4):219, January 2022.

- [3] Yue Luo, Gabriella D. Shepard, Jenny V. Ardelean, Daniel A. Rhodes, Bumho Kim, Katayun Barmak, James C. Hone, and Stefan Strauf. Deterministic coupling of site-controlled quantum emitters in monolayer WSe<sub>2</sub> to plasmonic nanocavities. Nature Nanotechnology, 13(12):1137, December 2018.
- [4] Tao Cai, Je-Hyung Kim, Zhili Yang, Subhojit Dutta, Shahriar Aghaeimeibodi, and Edo Waks. Radiative Enhancement of Single Quantum Emitters in WSe<sub>2</sub> Monolayers Using Site-Controlled Metallic Nanopillars. ACS Photonics, 5(9):3466, September 2018.
- [5] Frédéric Peyskens, Chitraleema Chakraborty, Muhammad Muneeb, Dries Van Thourhout, and Dirk Englund. Integration of single photon emitters in 2D layered materials with a silicon nitride photonic chip. Nature Communications, 10(1):4435, September 2019.
- [6] Oliver Iff, Quirin Buchinger, Magdalena Moczala-Dusanowska, Martin Kamp, Simon Betzold, Marcelo Davanco, Kartik Srinivasan, Sefaattin Tongay, Carlos Antón-Solanas, Sven Höfling, and Christian Schneider. Purcell-Enhanced Single Photon Source Based on a Deterministically Placed WSe<sub>2</sub> Monolayer Quantum Dot in a Circular Bragg Grating Cavity. Nano Letters, 21(11):4715, June 2021.
- [7] Jens-Christian Drawer, Victor Nikolaevich Mitryakhin, Hangyong Shan, Sven Stephan, Moritz Gittinger, Lukas Lackner, Bo Han, Gilbert Leibelng, Falk Eilenberger, Rounak Banerjee, Sefaattin Tongay, Kenji Watanabe, Takashi Taniguchi, Christoph Lienau, Martin Silies, Carlos Anton-Solanas, Martin Esmann, and Christian Schneider. Monolayer-Based Single-Photon Source in a Liquid-Helium-Free Open Cavity Featuring 65% Brightness and Quantum Coherence. Nano Letters, 23(18):8683, September 2023.
- [8] Luca Sortino, Panaiot G. Zotev, Catherine L. Phillips, Alistair J. Brash, Javier Cambiasso, Elena Marensi, A. Mark Fox, Stefan A. Maier, Riccardo Sapienza, and Alexander I. Tartakovskii. Bright single photon emitters with enhanced quantum efficiency in a two-dimensional semiconductor coupled with dielectric nano-antennas. Nature Communications, 12(1):6063, October 2021.

- [9] Arunabh Mukherjee, Chitraleema Chakraborty, Liangyu Qiu, and A. Nick Vamivakas. Electric field tuning of strain-induced quantum emitters in  $\text{WSe}_2$ . *AIP Advances*, 10(7):075310, 07 2020.
- [10] S Schwarz, A Kozikov, F Withers, J K Maguire, A P Foster, S Dufferwiel, L Hague, M N Makhonin, L R Wilson, A K Geim, K S Novoselov, and A I Tartakovskii. Electrically pumped single-defect light emitters in  $\text{WSe}_2$ . *2D Materials*, 3(2):025038, June 2016.
- [11] Shi Guo, Savvas Germanis, Takashi Taniguchi, Kenji Watanabe, Freddie Withers, and Isaac J. Luxmoore. Electrically Driven Site-Controlled Single Photon Source. *ACS Photonics*, 10(8):2549, August 2023.
- [12] Christopher E. Stevens, Hsun-Jen Chuang, Matthew R. Rosenberger, Kathleen M. McCreary, Chandriker Kavir Dass, Berend T. Jonker, and Joshua R. Hendrickson. Enhancing the Purity of Deterministically Placed Quantum Emitters in Monolayer  $\text{WSe}_2$ . *ACS Nano*, 16(12):20956, December 2022.
- [13] Jae-Pil So, Ha-Reem Kim, Hyeonjun Baek, Kwang-Yong Jeong, Hoo-Cheol Lee, Woong Huh, Yoon Seok Kim, Kenji Watanabe, Takashi Taniguchi, Jungkil Kim, Chul-Ho Lee, and Hong-Gyu Park. Electrically driven strain-induced deterministic single-photon emitters in a van der Waals heterostructure. *Science Advances*, 7(43):eabj3176, October 2021.
- [14] Carmen Palacios-Berraquero, Matteo Barbone, Dhiren M. Kara, Xiaolong Chen, Ilya Goykhman, Duhee Yoon, Anna K. Ott, Jan Beitner, Kenji Watanabe, Takashi Taniguchi, Andrea C. Ferrari, and Mete Atatüre. Atomically thin quantum light-emitting diodes. *Nature Communications*, 7(1):12978, September 2016.
- [15] Priya Johari and Vivek B. Shenoy. Tuning the Electronic Properties of Semiconducting Transition Metal Dichalcogenides by Applying Mechanical Strains. *ACS Nano*, 6(6):5449, June 2012.
- [16] Tingting Shen, Ashish V. Penumatcha, and Joerg Appenzeller. Strain Engineering for Transition Metal Dichalcogenides Based Field Effect Transistors. *ACS Nano*, 10(4):4712, April 2016.

- [17] Matthew Brooks and Guido Burkard. Theory of strain-induced confinement in transition metal dichalcogenide monolayers. Physical Review B, 97(19):195454, May 2018.
- [18] Moshe G. Harats, Jan N. Kirchof, Mengxiong Qiao, Kyrylo Greben, and Kirill I. Bolotin. Dynamics and efficient conversion of excitons to trions in non-uniformly strained monolayer WS<sub>2</sub>. Nature Photonics, 14(5):324, May 2020.
- [19] Iris Niehues, Robert Schmidt, Matthias Drüppel, Philipp Marauhn, Dominik Christiansen, Malte Selig, Gunnar Berghäuser, Daniel Wigger, Robert Schneider, Lisa Braasch, Rouven Koch, Andres Castellanos-Gomez, Tilmann Kuhn, Andreas Knorr, Ermin Malic, Michael Rohlfing, Steffen Michaelis De Vasconcellos, and Rudolf Bratschitsch. Strain Control of Exciton-Phonon Coupling in Atomically Thin Semiconductors. Nano Letters, 18(3):1751, March 2018.
- [20] Artur Branny, Santosh Kumar, Raphaël Proux, and Brian D Gerardot. Deterministic strain-induced arrays of quantum emitters in a two-dimensional semiconductor. Nature Communications, 8(1):15053, May 2017.
- [21] Carmen Palacios-Berraquero, Dhiren M. Kara, Alejandro R.-P. Montblanch, Matteo Barbone, Pawel Latawiec, Duhee Yoon, Anna K. Ott, Marko Loncar, Andrea C. Ferrari, and Mete Atatüre. Large-scale quantum-emitter arrays in atomically thin semiconductors. Nature Communications, 8(1):15093, May 2017.
- [22] Kamyar Parto, Shaimaa I. Azzam, Kaustav Banerjee, and Galan Moody. Defect and strain engineering of monolayer WSe<sub>2</sub> enables site-controlled single-photon emission up to 150 K. Nature Communications, 12(1):3585, June 2021.
- [23] Yue Luo, Na Liu, Xiangzhi Li, James C Hone, and Stefan Strauf. Single photon emission in WSe<sub>2</sub> up to 160 K by quantum yield control. 2D Materials, 6(3):035017, May 2019.
- [24] Jae-Pil So, Kwang-Yong Jeong, Jung Min Lee, Kyoung-Ho Kim, Soon-Jae Lee, Woong Huh, Ha-Reem Kim, Jae-Hyuck Choi, Jin Myung Kim, Yoon Seok Kim, Chul-Ho Lee, SungWoo Nam, and Hong-Gyu Park. Polarization Control of Deterministic Single-Photon Emitters in Monolayer WSe<sub>2</sub>. Nano Letters, 21(3):1546, February 2021.

- [25] S. Kumar, A. Kaczmarczyk, and B. D. Gerardot. Strain-Induced Spatial and Spectral Isolation of Quantum Emitters in Mono- and Bilayer WSe<sub>2</sub>. Nano Letters, 15(11):7567, November 2015.
- [26] L. C. Flatten, L. Weng, A. Branny, S. Johnson, P. R. Dolan, A. A. P. Trichet, B. D. Gerardot, and J. M. Smith. Microcavity enhanced single photon emission from two-dimensional WSe<sub>2</sub>. Applied Physics Letters, 112(19):191105, May 2018.
- [27] Thang B. Hoang, Gleb M. Akselrod, and Maiken H. Mikkelsen. Ultrafast Room-Temperature Single Photon Emission from Quantum Dots Coupled to Plasmonic Nanocavities. Nano Letters, 16(1):270, January 2016.
- [28] Luca Sapienza, Marcelo Davanço, Antonio Badolato, and Kartik Srinivasan. Nanoscale optical positioning of single quantum dots for bright and pure single-photon emission. Nature Communications, 6(1):7833, July 2015.
- [29] Igor Aharonovich, Dirk Englund, and Milos Toth. Solid-state single-photon emitters. Nature Photonics, 10(10):631, October 2016.
- [30] Sunny Gupta, Wenjing Wu, Shengxi Huang, and Boris I. Yakobson. Single-Photon Emission from Two-Dimensional Materials, to a Brighter Future. The Journal of Physical Chemistry Letters, 14(13):3274, April 2023.
- [31] Nicholas V. Proscia, Zav Shotan, Harishankar Jayakumar, Prithvi Reddy, Charles Cohen, Michael Dollar, Audrius Alkauskas, Marcus Doherty, Carlos A. Meriles, and Vinod M. Menon. Near-deterministic activation of room-temperature quantum emitters in hexagonal boron nitride. Optica, 5(9):1128, September 2018.
- [32] Yongjun Lee, Trang Thu Tran, Youngbum Kim, Shrawan Roy, Takashi Taniguchi, Kenji Watanabe, Joon I. Jang, and Jeongyong Kim. Enhanced Radiative Exciton Recombination in Monolayer WS<sub>2</sub> on the hBN Substrate Competing with Nonradiative Exciton-Exciton Annihilation. ACS Photonics, 9(3):873, March 2022.
- [33] Yusuke Hoshi, Takashi Kuroda, Mitsuhiro Okada, Rai Moriya, Satoru Masubuchi, Kenji Watanabe, Takashi Taniguchi, Ryo Kitaura, and Tomoki Machida. Suppression of exciton-

- exciton annihilation in tungsten disulfide monolayers encapsulated by hexagonal boron nitrides. Physical Review B, 95(24):241403, June 2017.
- [34] Suman Chatterjee, Garima Gupta, Sarthak Das, Kenji Watanabe, Takashi Taniguchi, and Kausik Majumdar. Trion-trion annihilation in monolayer WS<sub>2</sub>. Physical Review B, 105(12):L121409, March 2022.
- [35] Raghav Chaudhary, Varun Raghunathan, and Kausik Majumdar. Origin of selective enhancement of sharp defect emission lines in monolayer WSe<sub>2</sub> on rough metal substrate. Journal of Applied Physics, 127(7):073105, February 2020.
- [36] C. Simon, M. Afzelius, J. Appel, A. Boyer De La Giroday, S. J. Dewhurst, N. Gisin, C. Y. Hu, F. Jelezko, S. Kröll, J. H. Müller, J. Nunn, E. S. Polzik, J. G. Rarity, H. De Riedmatten, W. Rosenfeld, A. J. Shields, N. Sköld, R. M. Stevenson, R. Thew, I. A. Walmsley, M. C. Weber, H. Weinfurter, J. Wrachtrup, and R. J. Young. Quantum memories: A review based on the European integrated project “Qubit Applications (QAP)”. The European Physical Journal D, 58(1):1, May 2010.
- [37] Timm Gao, Martin Von Helversen, Carlos Antón-Solanas, Christian Schneider, and Tobias Heindel. Atomically-thin single-photon sources for quantum communication. npj 2D Materials and Applications, 7(1):4, January 2023.
- [38] Lintao Peng, Henry Chan, Priscilla Choo, Teri W. Odom, Subramanian K. R. S. Sankaranarayanan, and Xuedan Ma. Creation of Single-Photon Emitters in WSe<sub>2</sub> Monolayers Using Nanometer-Sized Gold Tips. Nano Letters, 20(8):5866, August 2020.
- [39] Qixing Wang, Julian Maisch, Fangdong Tang, Dong Zhao, Sheng Yang, Raphael Joos, Simone Luca Portalupi, Peter Michler, and Jurgen H. Smet. Highly Polarized Single Photons from Strain-Induced Quasi-1D Localized Excitons in WSe<sub>2</sub>. Nano Letters, 21(17):7175, September 2021.
- [40] Gabriella D Shepard, Obafunso A Ajayi, Xiangzhi Li, X-Y Zhu, James Hone, and Stefan Strauf. Nanobubble induced formation of quantum emitters in monolayer semiconductors. 2D Materials, 4(2):021019, March 2017.

- [41] Ajit Srivastava, Meinrad Sidler, Adrien V. Allain, Dominik S. Lembke, Andras Kis, and A. Imamoglu. Optically active quantum dots in monolayer WSe<sub>2</sub>. Nature Nanotechnology, 10(6):491, June 2015.
- [42] Matthew R. Rosenberger, Chandriker Kavir Dass, Hsun Jen Chuang, Saujan V. Sivaram, Kathleen M. McCreary, Joshua R. Hendrickson, and Berend T. Jonker. Quantum Calligraphy: Writing Single-Photon Emitters in a Two-Dimensional Materials Platform. ACS Nano, 13(1):904, 2019.
- [43] Pablo Hernández López, Sebastian Heeg, Christoph Schattauer, Sviatoslav Kovalchuk, Abhijeet Kumar, Douglas J. Bock, Jan N. Kirchhof, Bianca Höfer, Kyrylo Greben, Denis Yagodkin, Lukas Linhart, Florian Libisch, and Kirill I. Bolotin. Strain control of hybridization between dark and localized excitons in a 2D semiconductor. Nature Communications, 13(1):7691, December 2022.
- [44] Artem N. Abramov, Igor Y. Chestnov, Ekaterina S. Alimova, Tatiana Ivanova, Ivan S. Mukhin, Dmitry N. Krizhanovskii, Ivan A. Shelykh, Ivan V. Iorsh, and Vasily Kravtsov. Photoluminescence imaging of single photon emitters within nanoscale strain profiles in monolayer WSe<sub>2</sub>. Nature Communications, 14(1):5737, September 2023.
- [45] Hyowon Moon, Eric Bersin, Chitrleema Chakraborty, Ang-Yu Lu, Gabriele Grosso, Jing Kong, and Dirk Englund. Strain-Related Localized Exciton Energy in Atomically Thin Semiconductors. ACS Photonics, 7(5):1135, May 2020.
- [46] David D. Xu, Albert F. Vong, Dmitry Lebedev, Riddhi Ananth, Alexa M. Wong, Paul T. Brown, Mark C. Hersam, Chad A. Mirkin, and Emily A. Weiss. Conversion of Classical Light Emission from a Nanoparticle-Strained WSe<sub>2</sub> Monolayer into Quantum Light Emission via Electron Beam Irradiation. Advanced Materials, 35(5):2208066, February 2023.
- [47] Lukas Linhart, Matthias Paur, Valerie Smejkal, Joachim Burgdörfer, Thomas Mueller, and Florian Libisch. Localized Intervalley Defect Excitons as Single-Photon Emitters in WSe<sub>2</sub>. Physical Review Letters, 123(14):146401, September 2019.



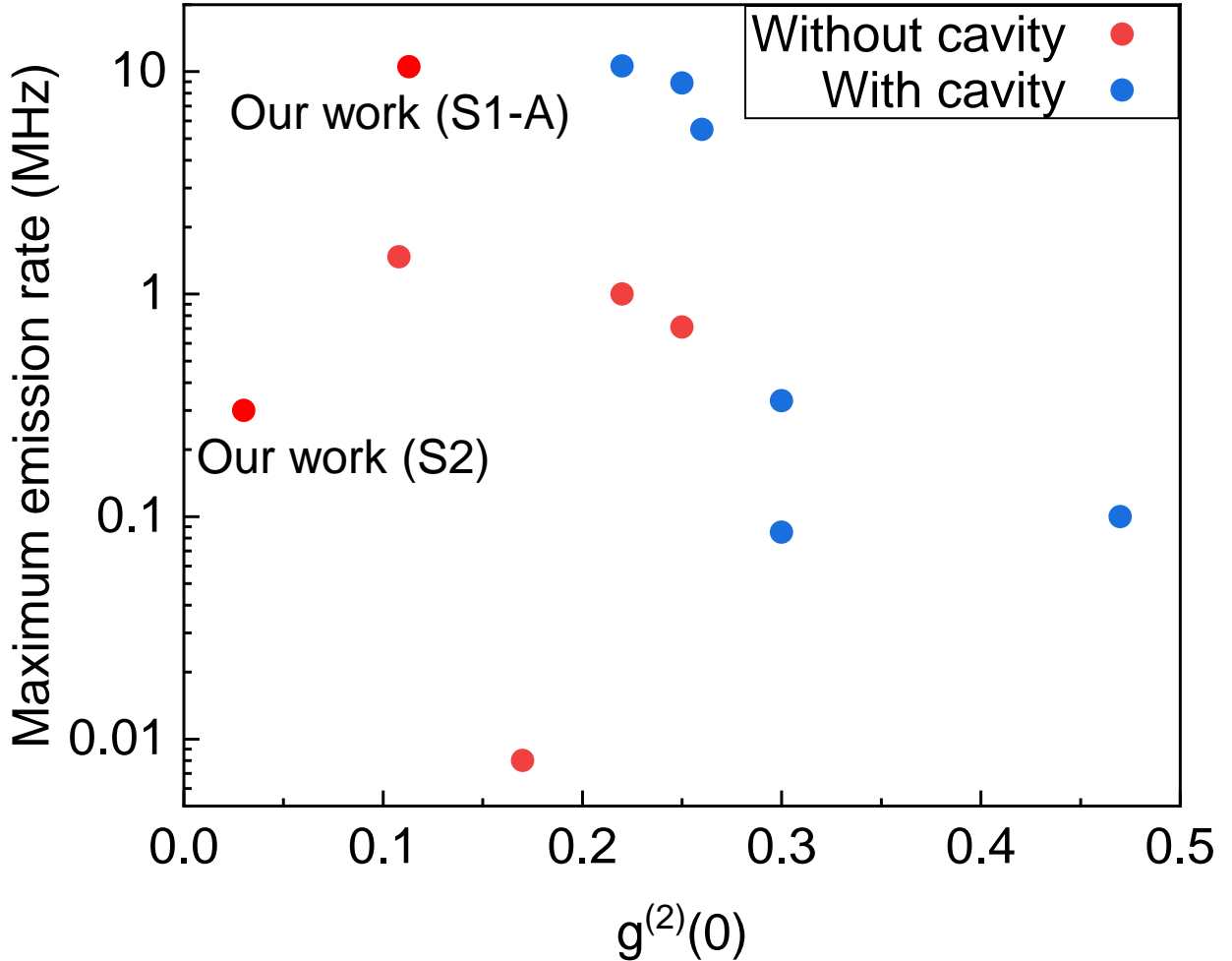


Figure 1: **Status of TMDC-based single photon emitters and benchmarking.** Brightness (in terms of maximum collected emission rate in MHz) against single photon purity [in terms of  $g^{(2)}(0)$ ] plotted for reported TMDC-based single photon emitters [3–5, 8, 24–26]. We have selected only those reports having scalable architecture and spatially deterministic SPE. Works implementing a photonic/plasmonic cavity are encoded in blue symbols, and those without cavities are encoded in red symbols. The plot also shows the results from this work having two different aspect ratios of pillars (samples S1-A and S2).

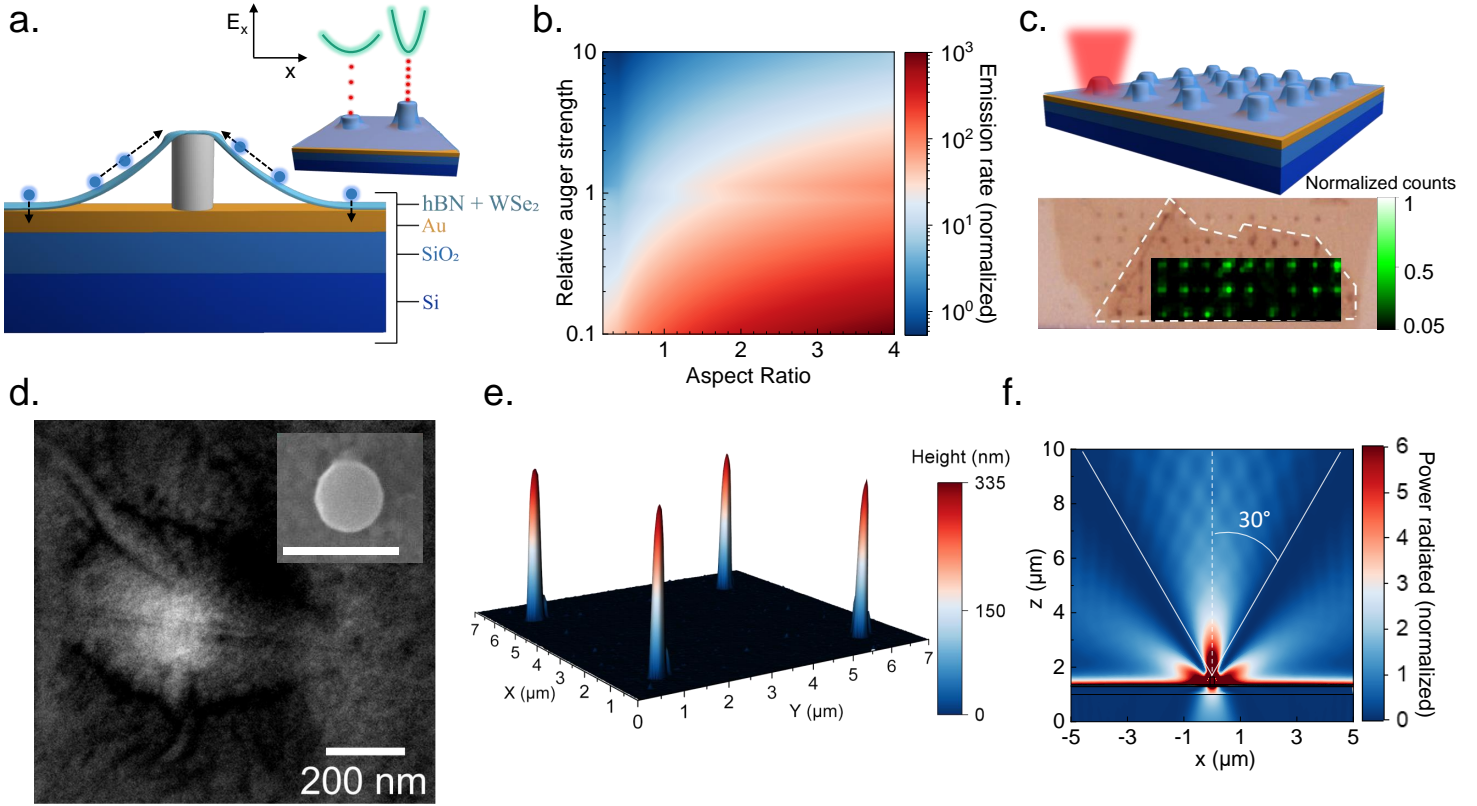


Figure 2: **Design of the single photon emitter.** **a** Schematic cross section showing the different layers in the SPE. Inset: Schematic showing a comparison of shorter versus taller pillars with respect to their single photon emission rates. Excitonic bands showing different band-bending gradients are also shown. **b** Colour plot from our model showing the variation of normalized maximum emission rate achievable as a function of the nanopillar aspect ratio and Auger coefficient. **c** Top panel: Schematic showing the array of nanopillars covered with TMD monolayer and hBN. Individual nanopillars are spaced by  $5 \mu\text{m}$  such that the excitation laser spot covers only one of the nanopillars. Bottom panel: Optical image of the fabricated device with  $\text{WSe}_2$  monolayer (bounded by white dashed line) covering the array of nanopillars. Overlaid is the result from the PL map showing bright emission spots coinciding with the nanopillar locations. **d** SEM image of the  $\text{WSe}_2$  monolayer on a nanopillar. The nanopillar touches the gold-coated substrate around 250-300 nm away from the center of the nanopillar. The scale bar is 200 nm. Inset: SEM image of a bare nanopillar showing a diameter of around 110 nm (scale bar is 200 nm). **e** AFM image of a section of the fabricated nanopillar array showing a set of 4 nanopillars with height around 330 nm. **f** Result from the FDTD simulation showing the spatial distribution of the emission pattern of the SPE on the pillar. The solid white lines indicate the collection angle of our objective with an NA of 0.5.

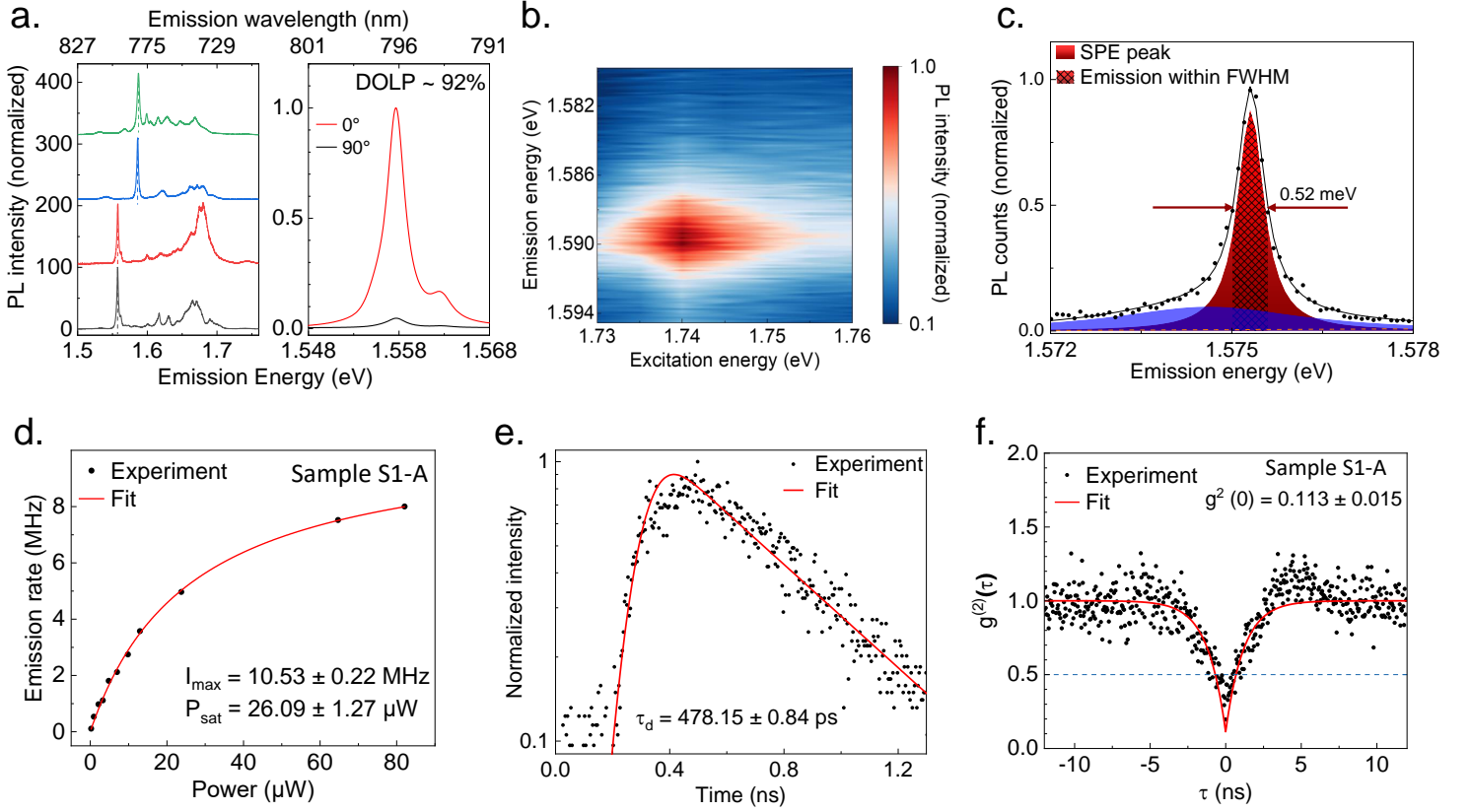


Figure 3: **Characterization of the single photon emitter.** **a** Left panel: PL spectra from four different nanopillar sites. The spectral location of the SPEs is marked by dashed vertical lines. Right panel: Polarization resolved PL spectrum of the SPE peak showing a DOLP of  $\sim 92\%$ . **b** Photoluminescence excitation measurement showing an enhancement in the SPE emission rate when the excitation is resonant to the free exciton energy of  $\text{WSe}_2$ . **c** Fitting of an SPE peak (data in black symbols and total fit in black solid trace) with Voigt functions and a background (orange dashed trace). The fitted peak (in red) is then integrated within its FWHM limits (black hatched portion) to calculate the integrated emission counts, thus removing the contribution from nearby peaks and background emission. The data shows a total measured line width of  $520 \mu\text{eV}$ . **d** Integrated emission count rate from **(c)** plotted as a function of excitation power. The data fits with a saturation equation, giving a maximum emission rate of  $10.53 \pm 0.22 \text{ MHz}$  and a saturation power of  $26.09 \mu\text{W}$ . **e** TRPL results (data in black symbols and fitting in red trace) to characterize the formation time and the lifetime of the defect state.  $t = 0$  marks the location of the laser pulse firing. **f** Second-order correlation measurement to quantify the purity of the SPE (experimental data in symbols and fitting in the red trace).

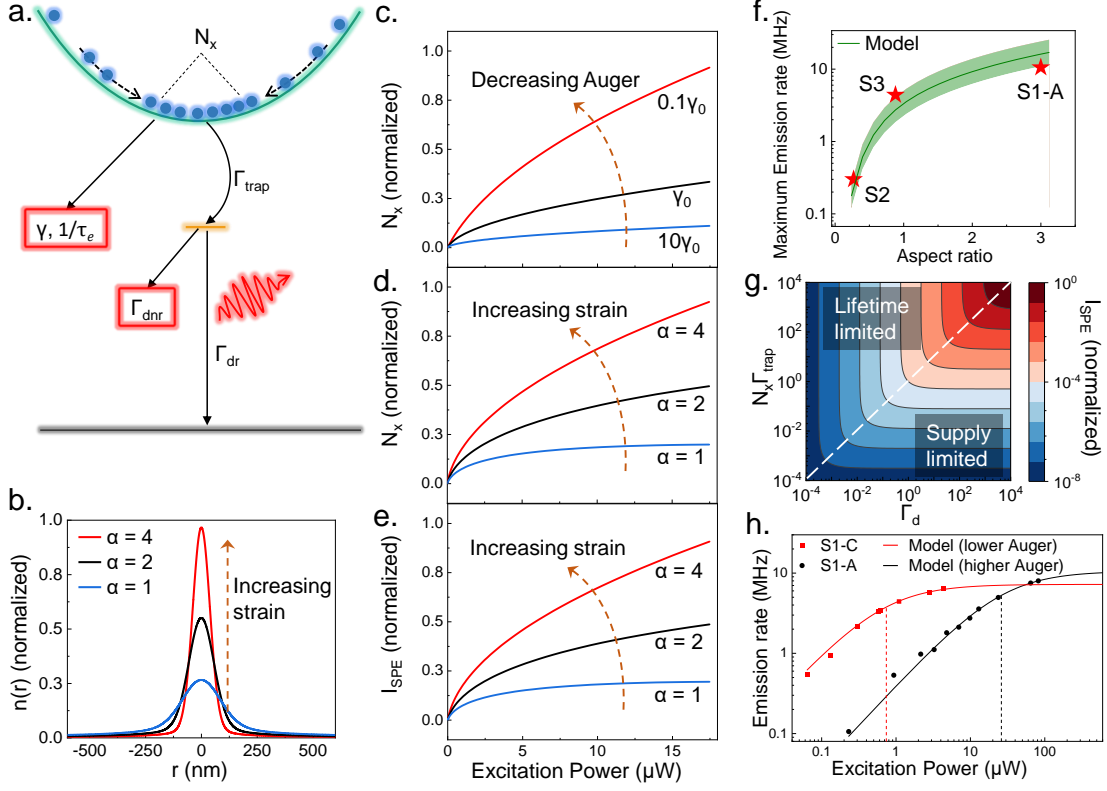


Figure 4: **Single photon emitter model.** **a** Schematic diagram showing the mechanism of exciton funneling in the strain-induced potential well and capture by the defect state. The processes involved at different stages are also illustrated. **b** Exciton density as a function of radial distance from the center of the pillar with varying pillar aspect ratio ( $\alpha$ ). **c-d** Exciton population near the center of the nanopillar ( $N_x$ ) as a function of excitation power with (c) varying Auger coefficient relative to a base value  $\gamma_0$  for a fixed aspect ratio of the pillar, and (d) varying aspect ratio of the pillar for a fixed Auger coefficient. **e** SPE emission intensity as a function of excitation power with a varying aspect ratio ( $\alpha$ ) of the pillar. **f** Fitting of the model (in the green trace) with the experimentally measured maximum emission rate from samples S1-A, S2, and S3 (in red star symbols) as a function of pillar aspect ratio. The shaded portion demonstrates a  $\pm 10\%$  variation in the model parameters. **g** Maximum SPE emission intensity (normalized) achievable by varying the supply to the defect state ( $N_x\Gamma_{trap}$ ) and total decay rate ( $\Gamma_d$ ) of the defect state, for a given quantum efficiency. The dashed line indicates  $\Gamma_d = N_x\Gamma_{trap}$  segregating the *supply-limited* regime from the *lifetime-limited* one. **h** Power dependent emission rate for S1-A (in black symbols) and S1-C (in red symbols) along with model fitting (solid traces). The fitted Auger coefficient for the red trace is about 100-fold smaller than the black trace. The dashed vertical lines indicate the corresponding saturation powers ( $0.74 \mu W$  for S1-C and  $26.09 \mu W$  for S1-A).

Supporting Information for:

Simultaneously enhancing brightness and purity of WSe<sub>2</sub> single photon emitter using high-aspect-ratio nanopillar array on metal

Mayank Chhaperwal<sup>1</sup>, Himanshu Madhukar Tongale<sup>1</sup>, Patrick Hays<sup>2</sup>, Kenji Watanabe<sup>3</sup>,  
Takashi Taniguchi<sup>4</sup>, Seth Ariel Tongay<sup>2</sup> and Kausik Majumdar<sup>1\*</sup>

<sup>1</sup>Department of Electrical Communication Engineering,  
Indian Institute of Science, Bangalore 560012, India

<sup>2</sup>Materials Science and Engineering, School for Engineering of Matter, Transport and Energy,  
Arizona State University, Tempe, Arizona 85287, USA

<sup>3</sup>Research Center for Electronic and Optical Materials,  
National Institute for Materials Science, 1-1 Namiki, Tsukuba 305-044, Japan

<sup>4</sup>Research Center for Materials Nanoarchitectonics,  
National Institute for Materials Science, 1-1 Namiki, Tsukuba 305-044, Japan

\*Corresponding author, email: kausikm@iisc.ac.in

# Supporting Information 1: Methods

## SPE fabrication

20/40 nm thick Ti/Au film is sputter coated on Si substrate covered with 285 nm thick thermally grown SiO<sub>2</sub>. A negative tone resist (ma-N-2403 from micro resist technology) is spin-coated on the substrate at 3000 rpm for 30 seconds to get a uniform layer of 300 nm thickness. The substrate is heated at 90°C for 2 minutes to cure the resist. A pattern with solid circles is defined on this substrate via electron beam lithography using an accelerating voltage of 30 kV and an aperture of 10  $\mu\text{m}$ . The diameter of the circles is kept at 150 nm, and an array is patterned with a spacing of 5  $\mu\text{m}$ . The electron beam hardens the negative resist in the location of the patterned circles. The substrate is then developed with AZ-726 MIF developer to remove the unwanted resist. The substrate is hard-baked at 150°C for 15 minutes to increase the mechanical strength of the nanopillars for transferring layers on top of them.

WSe<sub>2</sub> is exfoliated on a polydimethylsiloxane (PDMS) sheet and an appropriate monolayer flake is identified. We then use micro-manipulators to transfer this flake onto the patterned nanopillars. A few-layer thick hBN flake is then transferred on top using the same method. The entire structure is then annealed in vacuum ( $10^{-6}$  mbar) at 150°C for 3 hours.

## SPE Characterization

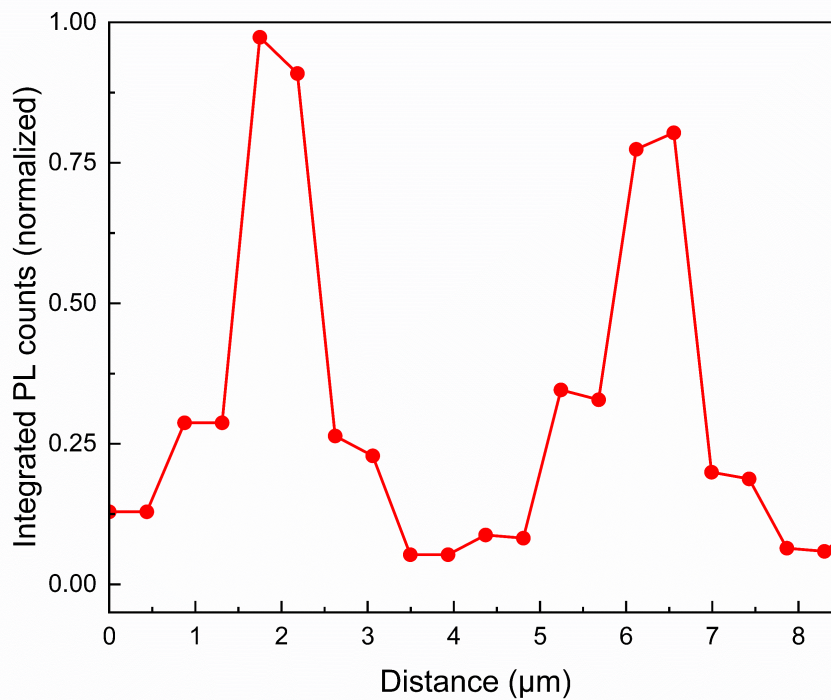
**Photoluminescence:** All PL measurements are carried out at 5 K temperature with a  $\times 50$  objective (numerical aperture of 0.5). The excitation source used is a 532 nm laser operated in CW mode unless otherwise stated. The spot size for the laser is  $\sim 1.5 \mu\text{m}$ . PL spectra are recorded with a spectrometer consisting of a grating with 1800 lines per mm and CCD. For the photoluminescence excitation (PLE) measurement, a supercontinuum source is used with a tunable narrow-band filter to vary the excitation wavelength.

**TRPL:** TRPL measurement is performed at 5 K with a 705 nm laser head (from PicoQuant) operated through a laser drive (PDL-800D) in pulsed mode with a 10 MHz repetition rate. Output from the SPE is guided to a single photon detector (SPD-050-CTC from Micro Photon Devices) via a combination of a long pass filter (cut in wavelength of 750 nm) and a tunable monochromator (Edmund optics) with a resolution of 0.5 nm. Time correlations are performed

by a time-correlated single photon counting (TCSPC) system (PicoHarp 300 from PicoQuant). The IRF of the entire TRPL setup is  $\sim 60$  ps. Data from the measurement is fitted with an exponential decay convoluted with a Gaussian rise function given by  $F(t) = \frac{1}{\sigma\sqrt{2\pi}} e^{-\frac{(t-\tau_f)^2}{2\sigma^2}}$  where  $\tau_f$  is the formation time measured from the laser excitation time.

**Second-order correlation:** second-order correlation measurements are performed with a CW excitation at 5 K. PL emission from the device is passed through a long pass filter (cut in wavelength of 750 nm) to remove the scattered laser component and then through a tunable monochromator (Edmund optics) with a resolution of 0.5 nm to select the SPE emission wavelength. The photons then go through a beamsplitter (from Thorlabs) and two single-photon detectors [from Excelitas] arranged in an HBT setup. The detectors are connected to the TCSPC system (PicoHarp 300 from PicoQuant), which generates a histogram of coincidence counts between the two outputs as a function of delay ( $\tau$ ) between them through QuCoo software (from PicoQuant). The plot is then normalized with respect to that of a coherence source such that the value of  $g^{(2)}(\tau)$  is 1 for  $\tau$  much larger than the lifetime of the emitter. Measured coincidences are normalized with that from a coherent source and are plotted in  $g^{(2)}(\tau)$  with varying delay ( $\tau$ ) between the two detectors. The timing jitter (250 ps) of the SPADs, being comparable to  $\tau_d$ , modifies the slope and the value of the anti-bunching dip. The  $g^{(2)}(\tau)$  curve is then deconvoluted from the Gaussian instrument response function (IRF) of the HBT setup arising from the finite timing jitter of the detectors (250 ps each) and the finite bin size used in the QuCoo software for calculating the correlation (50 ps for the measurement at higher emission rate and 100 ps for the measurement at lower emission rate).

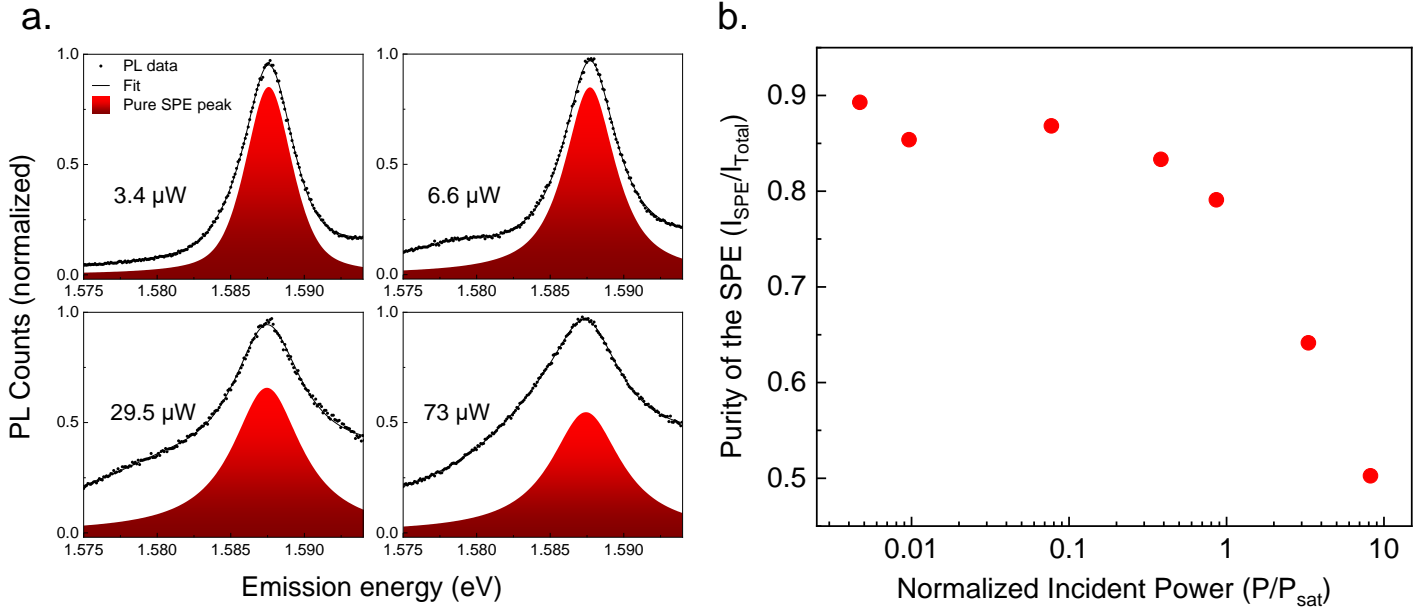
## Supporting Information 2: Line cut from the PL map



Supporting Figure 1: **Line cut from the PL map.** Integrated exciton emission taken from two of the brightest nanopillars from the PL map show the suppression of emissions from the flat regions compared to that from the nanopillars.



### Supporting Information 3: Measurement of count rate: SPAD count rate versus pure SPE count rate

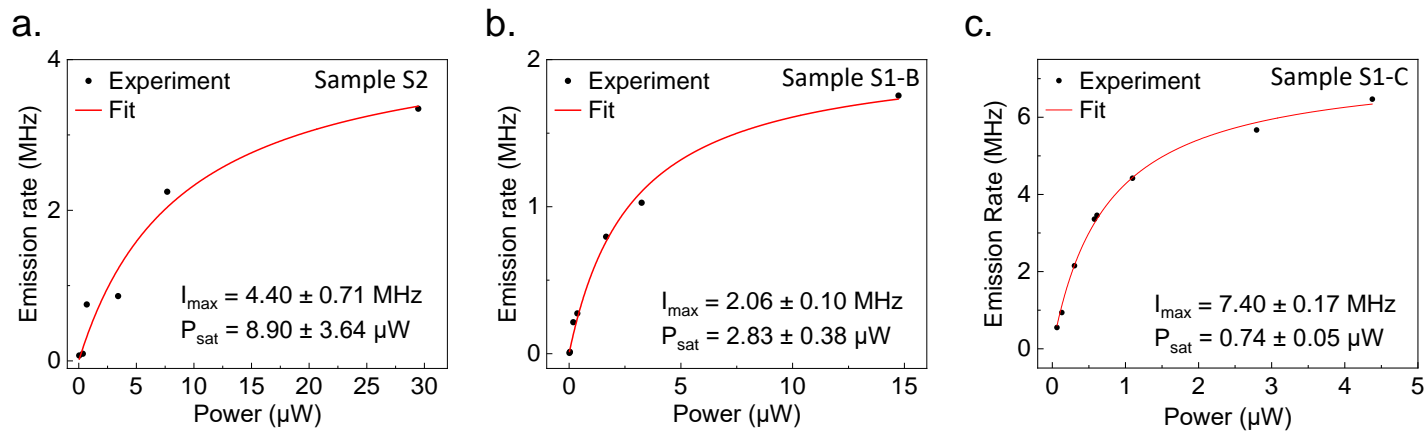


Supporting Figure 2: **variation of SPE purity with incident power.** **a** PL spectra from one of the pillars taken at four different incident power values. Measured PL data in black symbols, the black trace is fit to the data, and the shaded red peak is the fitted SPE peak after the removal of the contribution from the side peaks and background. **b** Ratio of the SPE intensity and the total intensity (integrated up to the FWHM). The ratio directly correlates with the purity of the photons collected by the SPAD.

Figure 2a shows the rise in the non-SPE emission with increasing incident power for one of the nanopillars. Since the SPE has a strong saturating behavior and the background emission does not, the gap between the total and pure SPE emissions widens as the incident power increases. PL counts for this device are integrated within its FWHM for both the raw PL and the fitted SPE peak (contributions from other sources removed). Since the counts measured by the SPAD correspond to the raw PL counts, we plot the ratio of SPE counts to that of SPAD

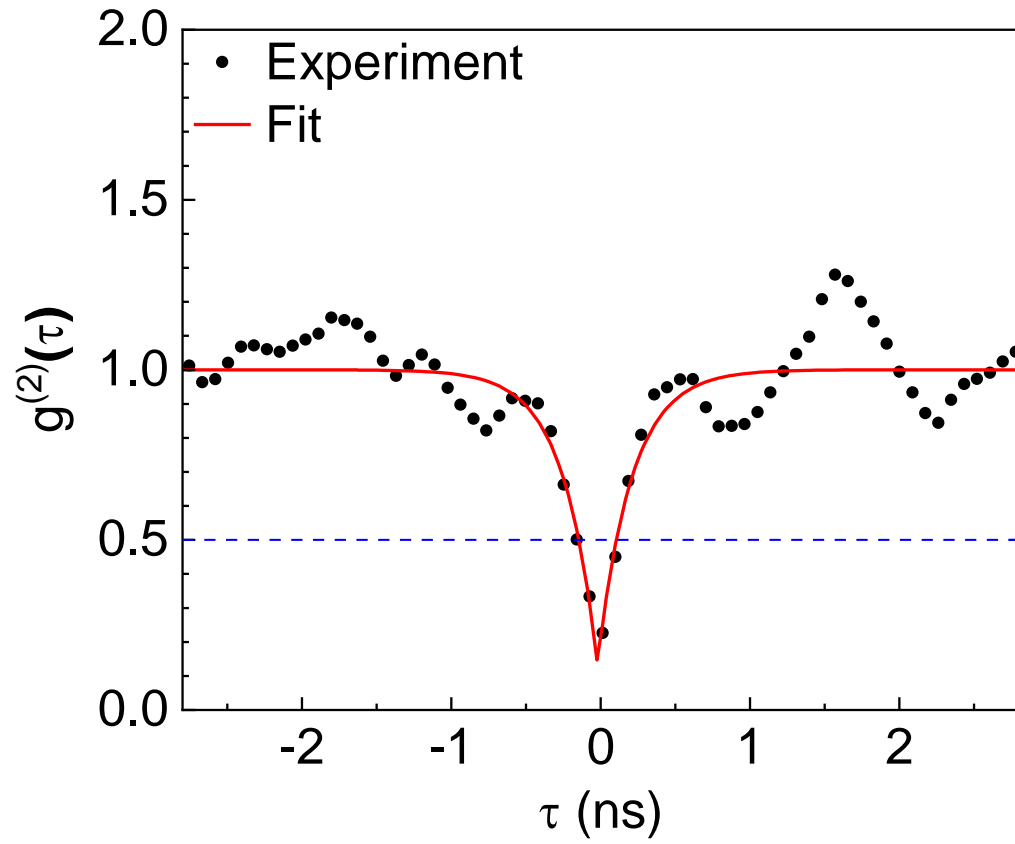
counts in Figure 2b. The rapid decrease in the purity of the counts measured by the SPAD with incident power shows that SPAD counts can erroneously inflate the emission rate such that only a fraction of the measured photons are from the SPE. Note that this data is taken from our sample with SPE peak red-shifted compared to broad defect emission of WSe<sub>2</sub> and has a gold-coated substrate, which cuts down the background emission to a good extent. Thus, this ratio can be even worse for other device designs.

## Supporting Information 4: High emission rate from more samples



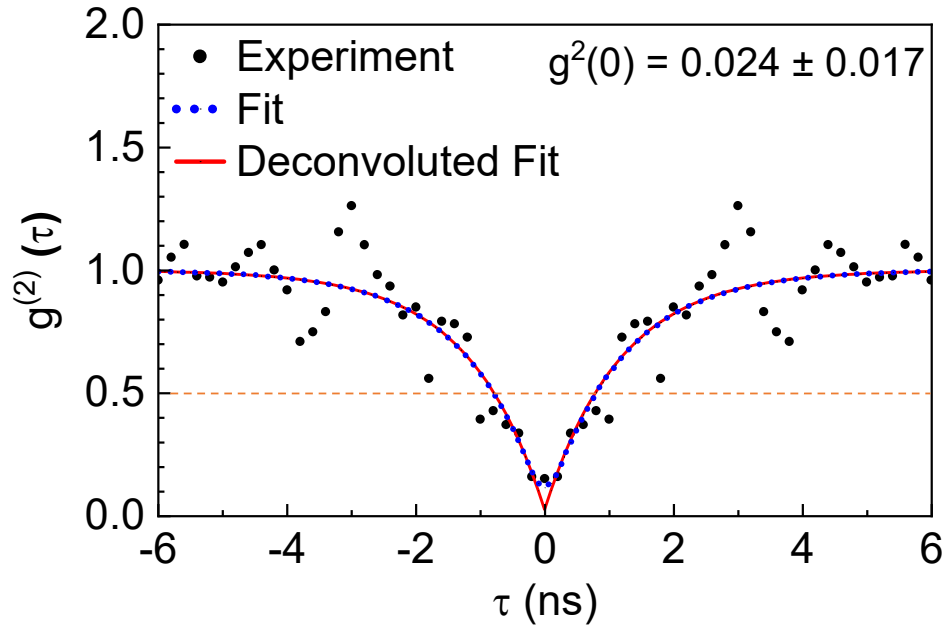
Supporting Figure 3: **Power dependent Emission rate from multiple samples.** a-c Integrated (within FWHM) emission rate measured for 3 different samples apart from the ones presented in the main text.

Supporting Information 5:  $g^{(2)}(\tau)$  from SPE shown in Figure 3c  
in main text



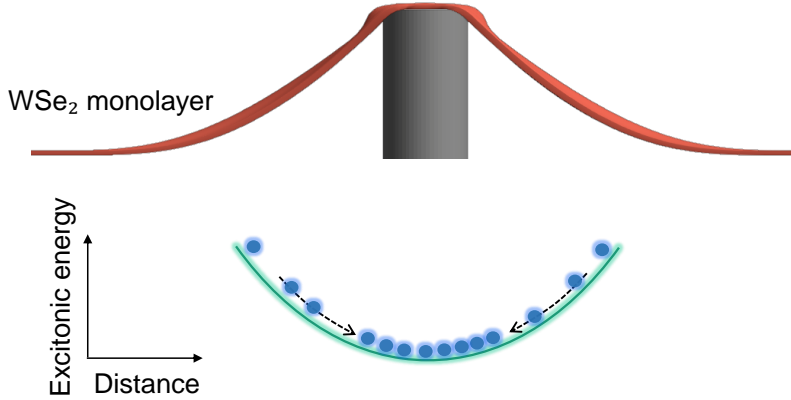
Supporting Figure 4:  $g^{(2)}(\tau)$  from SPE shown in Figure 3c in main text. Second-order correlation measurement for the device with linewidth of  $520 \mu\text{eV}$ . Experimental data in symbols, fitting in solid red trace.

Supporting Information 6:  $g^{(2)}(0)$  from a device with lower aspect ratio (sample S2)



Supporting Figure 5:  $g^{(2)}(\tau)$  from a device with lower aspect ratio (sample S2). Second-order correlation measurement for the device with lower aspect ratio of 0.27 (sample S2). Experimental data in symbols, fitting in the blue dots and deconvoluted curve in solid red trace. The  $g^{(2)}(0)$  value obtained after deconvolution is  $0.024 \pm 0.017$ , which is well below 0.5 (indicated by dashed orange line)

## Supporting Information 7: Exciton dynamics in a strain-induced potential well



Supporting Figure 6: **Bandgap modulation and exciton dynamics under non-uniform strain** Top panel: Schematic showing a WSe<sub>2</sub> monolayer placed on a nanopillar. The TMD bends and undergoes non-uniform strain that is maximum at the center of the nanopillar. Bottom panel: Excitonic band bending due to the non-uniform strain. Excitons (blue balls) funnel to the energy minimum at the center of the nanopillar (shown by black dashed arrows).

Placing a WSe<sub>2</sub> monolayer on a nanopillar bends the monolayer introducing a non-uniform strain which is maximum on the nanopillar and gradually reduces to zero value when the flake is in contact with the substrate (See Supplementary Figure 6). The bandgap of the WSe<sub>2</sub> monolayer reduces proportional to the amount of strain applied. Thus, the bandgap minimum coincides with the center of the nanopillar in real space. Exciton band can thus be modeled as a spatially parabolic function, 2D equivalent of which is shown in Supplementary Figure 6. Excitonic energy in this parabolic band can be modeled as:

$$E_x(r) = E_{min} + \frac{1}{2}kr^2 \quad (1)$$

where  $E_{min}$  is the minimum of the excitonic energy at the center of the nanopillar where the

strain is maximum,  $r$  is the radial distance away from the center of the nanopillar, and  $k$  correlates the gradient of excitonic band bending with the strain gradient and is proportional to the aspect ratio ( $\alpha$ ) of the nanopillar for any particular diameter. To calibrate  $k$  with  $\alpha$  for the model, the strain-dependent change in excitonic energy is taken to be varying from 30.8 meV (at the center of the nanopillar) to 0 meV (at a distance of 250 nm away from the nanopillar) for an aspect ratio of 0.59. [1]

The induced electric field due to the band bending is given by:

$$E_{in}(r) = \frac{-1}{e} \frac{\partial E_x}{\partial r} \quad (2)$$

where  $e$  is the electronic charge.

The total flux of the excitons in the system consists of both drift towards the center (due to the gradient in bandgap) and diffusion away from the center (due to exciton concentration gradient arising from the Gaussian generation profile of the laser) and is given by:

$$F = \mu_e n E_{in} - D_e \frac{\partial n}{\partial r} \quad (3)$$

where  $\mu_e$  and  $D_e$  are the mobility and diffusion coefficient of the excitons in the strain-induced potential well, respectively and  $n$  is the exciton density.

Including other exciton gain and loss mechanisms such as Gaussian generation profile of the laser [ $g(r)$ , a function of the excitation power  $P$ ], recombination of excitons with an effective lifetime of  $\tau$ , and Auger annihilation (with coefficient  $\gamma$ ), the final rate equation governing the dynamics of the excitons in the system is given by:

$$\frac{\partial n(r, t)}{\partial t} = -\frac{\partial F}{\partial r} + g(r) - \frac{n(r)}{\tau_e} - \gamma n^2(r) \quad (4)$$

At steady state ( $\frac{\partial n(r, t)}{\partial t} = 0$ ), the equation becomes:

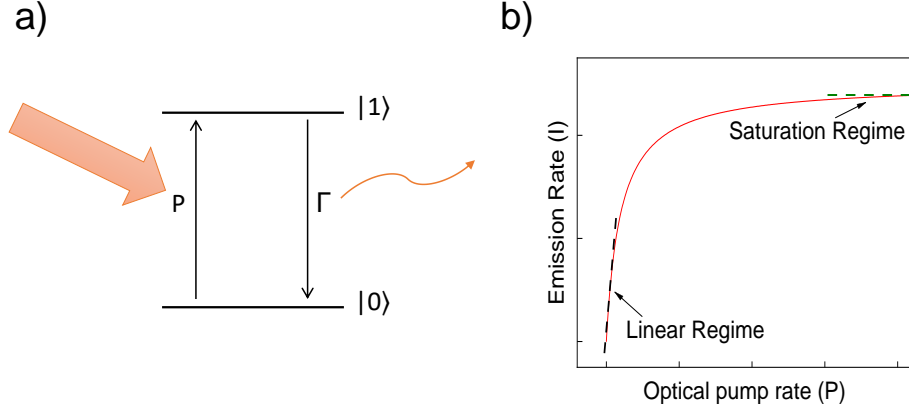
$$\frac{\partial F}{\partial r} = g(r) - \frac{n(r)}{\tau_e} - \gamma n^2(r) \quad (5)$$

This equation (coupled with Equation 3) was discretized by converting differentials to forward differences and was numerically solved in MATLAB to find the exciton density distribution

$[n(r)]$  as a function of  $r$ . Values of  $\mu_e$ ,  $D_e$ , and  $\gamma$  are taken from literature [2–4]. To generate the plots, we assume a nanopillar diameter of 100 nm and vary the height of the nanopillar to get different aspect ratios.



## Supporting Information 8: A generic two-level emitter



Supporting Figure 7: **A generic 2-level system.** **a** Excited state  $|1\rangle$  and ground state  $|0\rangle$  of a 2-level emitter with a pump rate  $P$  and a recombination rate  $\Gamma$ . **b** Emission rate as a function of excitation power. Black dashed line shows the linear region where  $P \ll \Gamma$ . Green dashed line shows the saturation region where  $P \gg \Gamma$ .

Consider a two-level system with ground state  $|0\rangle$  and excited state  $|1\rangle$ , as shown in Supplementary Figure 7a. The System is optically pumped from  $|0\rangle$  to  $|1\rangle$ . The effective pumping rate is  $P$  which gives a formation time for the excited state of  $\tau_f = 1/P$ . The system then relaxes to its ground state. Relaxation can be through radiative or non-radiative pathways.  $\tau$  is the effective lifetime of the state  $|1\rangle$ , taking both pathways into account. The effective relaxation rate for the system is then  $\Gamma = 1/\tau$ . Considering  $\rho_1$  and  $\rho_0$  to be the occupation probabilities of the excited state and ground state, respectively, the coupled rate equations for the system can be written as:

$$\frac{d\rho_1}{dt} = \rho_0 P - \rho_1 \Gamma \quad (6)$$

$$\frac{d\rho_0}{dt} = \rho_1 \Gamma - \rho_0 P \quad (7)$$

Since these two states are the only possible states of the system,  $\rho_1 + \rho_0 = 1$ . Using this

relation and considering steady state, the pair of equations (6) and (7) can be solved to get:

$$\rho_1 = \frac{P}{P + \Gamma} \quad (8)$$

Steady state emission rate of a two-level system is directly proportional to occupation probability of its excited state, therefore:

$$I \propto \frac{P}{P + \Gamma} \implies I = I_{max} \left( \frac{P}{P + \Gamma} \right) \quad (9)$$

Where  $I_{max}$  is the maximum emission rate of the system, limited by its lifetime. When  $P \ll \Gamma$ , such that  $P + \Gamma \approx \Gamma$ , we have  $I \approx (I_{max}/\Gamma)P$  resulting in linearity in emission vs excitation power plot (black dashed line in Supplementary Figure 7b) for small values of  $P$ . After increasing the excitation power much further, we reach a limit where  $P \gg \Gamma$ , such that  $P + \Gamma \approx P$ . At this point,  $I \approx I_{max}$ , and we see a saturation behavior in the intensity versus excitation power plot (green dashed line in Supplementary Figure 7b).

## Supporting Information 9: A Defect-based SPE coupled with an exciton reservoir

The rate of the exciton capture depends on the capture probability of individual exciton and  $N_x$ . Once the defect state is empty, another exciton from the excitonic band can be captured, and the process continues. If the supply of excitons in the reservoir is maintained, it emits a stream of single photons. We consider an occupation probability  $\rho_d$  of the defect state such that  $0 \leq \rho_d \leq 1$ . Trapping of exciton from the excitonic band into the defect can be modeled as the filling of this defect state via the exciton reservoir. The rate of this filling is  $(1 - \rho_d)N_x\Gamma_{trap}$ , where  $N_x$  is the exciton reservoir population i.e. the total exciton population near the defect within its capture cross-section,  $\Gamma_{trap}$  is the rate of exciton trapping, and  $(1 - \rho_d)$  is the probability of the defect state being unoccupied. This term ensures that the probability of capture of another exciton when the defect is already occupied is zero. Similarly, the rate of emptying of the defect state is  $\rho_d\Gamma_d$ , where  $\Gamma_d$  is the electron-hole recombination rate through both radiative and non-radiative pathways and is inverse of the effective lifetime  $\tau_d$  of the defect state.

Combining both of these factors, the rate equation for our SPE two-level system is given by:

$$\frac{d\rho_d}{dt} = (1 - \rho_d)N_x\Gamma_{trap} - \rho_d\Gamma_d \quad (10)$$

At steady state  $\frac{d\rho_d}{dt} = 0$  which results in the following solution:

$$\rho_d = \frac{N_x\Gamma_{trap}}{N_x\Gamma_{trap} + \Gamma_d} \quad (11)$$

Emission rate of the system is proportional to both the occupation probability ( $\rho_d$ ) of its excited state and the radiative decay rate of the excited state ( $\Gamma_{dr}$ ). Thus it is given by:

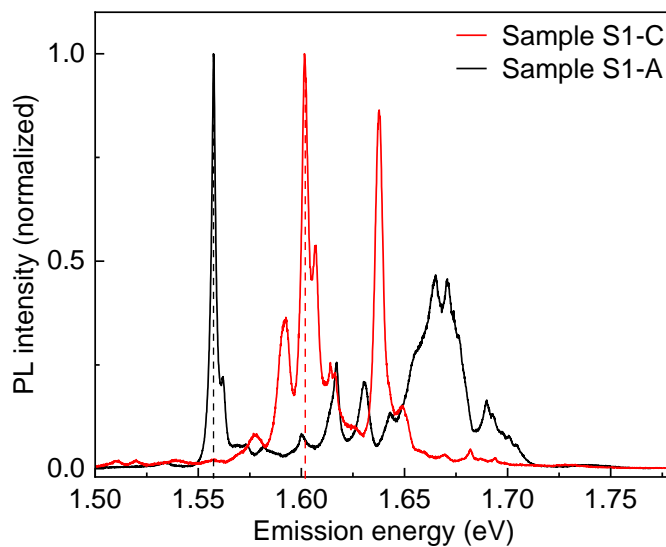
$$I_{SPE} = \Gamma_{dr} \left( \frac{N_x\Gamma_{trap}}{N_x\Gamma_{trap} + \Gamma_d} \right) \quad (12)$$

Thus, the maximum achievable rate for the SPE is the radiative lifetime limited rate of  $\Gamma_{dr}$ .

Note that the term  $N_x\Gamma_{trap}$  in Equation 12 is analogous to the Pump rate term  $P$  in

Equation 9. Therefore, the formation time here can be approximated as  $\tau_f \approx \frac{1}{N_x \Gamma_{trap}}$ . An important distinction between the two is that this term can not be increased to an arbitrary value by increasing the optical excitation power. This is because of the saturation of  $N_x$ , as demonstrated in subsystem 1 of the model. Therefore the condition of  $N_x \Gamma_{trap} \gg \Gamma_d$  (analogous to  $P \gg \Gamma$  in Supporting Information 5) is often difficult to achieve.

## Supporting Information 10: Comparison of devices with higher and lower Auger coefficients



Supporting Figure 8: **Comparison of devices with higher and lower Auger coefficients.** Suppression of background defect emission analyzed through PL emission for the device fabricated with a different batch of WSe<sub>2</sub> (sample S1-C, in red) when compared to the device presented in the main text (sample S1-A, in black).

## References

- [1] Artur Branny, Santosh Kumar, Raphaël Proux, and Brian D Gerardot. Deterministic strain-induced arrays of quantum emitters in a two-dimensional semiconductor. Nature Communications, 8(1):15053, May 2017.
- [2] F. Cadiz, C. Robert, E. Courtade, M. Manca, L. Martinelli, T. Taniguchi, K. Watanabe, T. Amand, A. C. H. Rowe, D. Paget, B. Urbaszek, and X. Marie. Exciton diffusion in WSe<sub>2</sub> monolayers embedded in a van der Waals heterostructure. Applied Physics Letters, 112(15):152106, April 2018.
- [3] Florian Dirnberger, Jonas D. Ziegler, Paulo E. Faria Junior, Rezlind Bushati, Takashi Taniguchi, Kenji Watanabe, Jaroslav Fabian, Dominique Bougeard, Alexey Chernikov, and Vinod M. Menon. Quasi-1D exciton channels in strain-engineered 2D materials. Science Advances, 7(44):eabj3066, October 2021.
- [4] Long Yuan and Libai Huang. Exciton dynamics and annihilation in WS<sub>2</sub> 2D semiconductors. Nanoscale, 7(16):7402, 2015.